Journal of Materials Chemistry A

Accepted Manuscript

This article can be cited before page numbers have been issued, to do this please use: P. Qin, J. Zhang, G. Yang, X. Yu and G. Li, *J. Mater. Chem. A*, 2018, DOI: 10.1039/C8TA09026B.

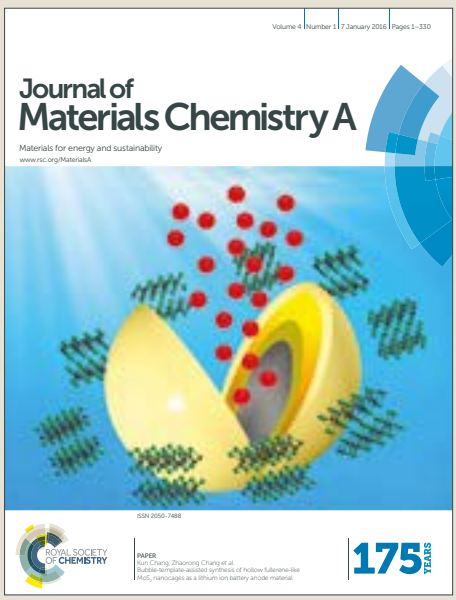

ROYAL SOCIETY OF CHEMISTRY

rsc.li/materials-a

View Article Online
DOI: 10.1039/C8TA09026B

Potassium-intercalated rubrene as dual-functional passivate agent for high efficiency perovskite solar cells

Pingli Qin*[a,b], Jiliang Zhang[c], Guang Yang[a], Xueli Yu[b], and Gang Li*[a]

[a] The Department of Electronic and Information Engineering, the Hong Kong Polytechnic University, Hong Hum, Kowloon, Hong Kong SAR, China
[b] Hubei Key Laboratory of Optical Information and Pattern Recognition, Wuhan Institute of Technology, Wuhan, Hubei 430205, P. R. China
[c] Department of Energy and Materials Engineering, Dongguk University, Seoul 04620 South Korea

E-mail: gang.w.li@polyu.edu.hk; qpl2015@wit.edu.cn

View Article Online
DOI: 10.1039/C8TA09026B

Abstract:

The defects and related trap sites are generated inevitably at grain boundaries (GBs) and on surfaces of solution-processed polycrystalline perovskite films. Seeking the suitable passivation material with facial and efficient methods to passivate the perovskite film for minimum defect density is necessary for further improving the photovoltaic performance. Here, we introduce a novel potassium-intercalated rubrene (K_2Rubrene) with a facile anti-solvent engineering to obtain high quality perovskite films through a novel dual-functional perovskite passivation approach. It was found that the cation–π interaction between aromatic rubrene and organic cations can immobilize the organic cations in perovskite, which could trigger some heterogeneous nucleation over the perovskite precursor film to decrease the grain size and obtain more homogeneous and uniform perovskite film. The potassium insertion in K_2Rubrene molecule, more importantly, could balance the cation–π interaction energy that occurred between aromatic additive and the organic cations in perovskite films to reduce the barrier for the better carrier transfer at GBs. Moreover, K^+ could enter freely the A-site defects at surface of the perovskite absorber and then digest the A-site shallow defects to prevent the migration & autorotation of the large organic cations at interface between the hole transfer layer and the perovskite absorber, or perovskite/perovskite GBs. Consequently, a significant upshift of valence band maximum and conduction band minimum of the perovskite material leads to a more favorable energy alignment with hole transporting material, which can enhance the hole-transfer and suppress the hysteresis, and the corresponding perovskite solar cell device achieves a high-efficiency over 19%, higher than those of the pristine and rubrene based devices.

Keywords: K_2Rubrene; interface; trap-passivation; potassium insertion; perovskite solar cells

View Article Online
DOI: 10.1039/C8TA09026B

Introduction

Recently, milestone works in materials and device configuration, such as the first embodiment use of hybrid organo-metal halide perovskite in a liquid electrolyte device configuration, the perovskite quantum-dot coating protocol in electrolyte-based sensitizer configuration,[1] the solid-state sensitized configuration,[2, 3] a mesoporous alumina scaffold in planar heterojunction configuration[4] and various passivation approaches etc., the perovskite solar cells (PSCs) have exhibited externally verified power conversion efficiencies (PCE) exceeding 23% outclass from 3.8% in 2009.[5, 6] It is realized that these astounding progresses are related to many reasonable engineering that manipulates the perovskite morphology and optimize interfacial nature function.[7] The film morphologies of the perovskite photoactive layer, including grain boundaries (GBs), grain size & distribution, surface coverage, and crystal orientation, play crucial roles on the performance of the completed devices. Electronic trap states are typically determined by the GBs, and are tunable based on the material compositions and processing conditions. These traps can enhance non-radiative recombination and reduce seriously charge carrier lifetime and photoluminescence (PL) yield. To obtain the high quality perovskite films with full coverage and fewer GBs, many approaches, such as one-step spin-coating,[3, 8, 9] sequential deposition,[10-12] co-evaporation,[4, 13-15] vapor assisted solution process,[16-18 19] additive or solvent annealing engineering,[20-27] have been adopted to reduce the electronic trap states in perovskite photoactive layer. One-step spin coating is the most common method to make the precursors onto the substrate for the perovskite crystalline film through solvent evaporation in the lab. However, it

View Article Online
DOI: 10.1039/C8TA09026B

is very hard to control the nucleation and growth of the perovskite crystal during the process because of the fast solvent evaporation or rapid reaction between the lead source (e.g. PbI_2) and halogenated amine (e.g. CH_3NH_3I). Consequently, many pinholes or GBs within the final perovskite film will form and lead to the low coverage with the poor morphology perovskite photoactive layer.[22]

It has been reported that the control of the nucleation and growth can improve the morphology of the perovskite photoactive layer during the process of the perovskite crystal formation for the high PCE of PSCs.[20, 21, 28, 29] Another important strategy to improve the efficiency of these PSCs' device is minimizing the charge recombination by passivating the dangling bonds at surfaces and GBs. Metal ions and organic additives doping are two main passivation techniques used in the field of PSCs. [20, 21, 28, 30-33] The incorporation of metal ions can modulate the perovskite crystallization process and therefore the film morphology. Snaith and co-workers have found that a small quantity of Al^{3+} doping can enhance the PCE and reduce the hysteresis; and recently Strank and co-workers showed potassium doping can effectively passivate perovskite defects, reducing non-radiative recombination loss and thus achieve high performance PSCs.[34-36]

The organic additives, such as, dimethyl sulfoxide (DMSO), 1, 8-diiodooctane, methylammonium acetate and thiosemicarbazide,[23-26, 37] have been widely used to form intermediate adducts with Pb^{2+} to slow down the crystal growth, suggesting that it could passivate the surface recombination sites with undercoordinated Pb sites by a typical Lewis base to minimize the number of defects.[20, 21, 28, 29] However, these postgrowth

View Article Online
DOI: 10.1039/C8TA09026B

treatments are challenging to yield reproducible results due to the uneven dispersion of the organic additive in the perovskite precursor solution. Moreover, some pristine organic semiconducting molecules have an intrinsically low carrier-mobility and -conductivity. Although the addition of functionalized dopants, such as lithium salt[38, 39], copper salts [40] carbon nanotubes[41] and some p-type additives,[42] into organic semiconducting molecules solution can enhance the conductivity, these additives suffer aggregation problems in achieving reliable electrical conductivity enhancement.[43]

Another way to obtain high quality perovskite is rapid nucleation.[20, 21, 28] It has been confirmed that anti-solvent method can induce rapid nucleation to suppress molecules/additives from aggregation and trigger effectively a homogeneous nucleation at the surface of the formed layer. This then forms a typical Lewis based intermediate adducts with undercoordinated Pb to passivate the defect at the interfaces, surfaces or GBs within the final perovskite film.[20, 21] Using the technique, Li et al. have found that the cation–π interaction between aromatic rubrene and organic cations is strong enough to immobilize the organic cations in perovskite, lead to the reduction of defects in perovskite films, and they achieved outstanding stability in devices.[44] Here, we introduce potassium-intercalated rubrene (K_2Rubrene) material as a template-agent to control the nucleation. Meanwhile, K_2Rubrene can suppress the aggregation, and the K^+ cations can efficiently passivate the perovskite interface traps, which is also beneficial to improve the hole-extraction and hole–transporting capability of hole-transporting layer (HTL). Compared to common organic fullerene derivatives, K_2Rubrene salts are sparingly soluble in chlorobenzene, satisfying the precondition of

View Article Online
DOI: 10.1039/C8TA09026B

being passivation materials. Based on the mixed ternary cation perovskite $(CsI)_{0.04}(FAI)_{0.82}(PbI_2)_{0.86}(MAPbBr_3)_{0.14}$ (Cs=cesium, MA=methylammonium, CH_3NH_3, and FA = formamidinium, $CH_3(NH_2)_2$) system, the PSC devices based on K_2Rubrene delivered the average PCE of 18.56%, which is higher than that of the control device (17.82%), and the device employing rubrene as an additive in anti-solvent CB (16.43%). These results represent a new simple approach for new passivation material design for the improvement of the properties of PSC devices.

Experimental

Materials

Fluorine-doped tin oxide (FTO) glass substrates with a sheet resistance of 14 Ω/sq were supplied from Asahi Glass (Japan). Methylammonium bromide (MABr) and formamidinium iodide (FAI) were purchased from Dyesol. Lead (II) bromide ($PbBr_2$, 99.99%), Cesium iodide (CsI, 99.99%), bis(trifluoromethane) sulfonimide lithium salt (Li-TFSI, 99%), poly (3, 4-ethylenedioxythiophene): poly (styrenesulfonate) (PEDOT:PSS) and 4-tert-butylpyridine (TBP, 96%) were purchased from Xi'an Polymer Light Technology Corp. Tin(II) chloride dehydrate($SnCl_2 \cdot 2H_2O$), thiourea, dimethyl sulfoxide (DMSO), N, N-dimethylformamide (DMF), acetonitrile， K chunks (99.99%), rubrene powder (sublimed grade, 99.9%) and chlorobenzene (CB) were purchased from Sigma-Aldrich. Lead (II) iodide (PbI_2, 99.8%) was purchased from TCI while spiro-MeOTAD [2,2,7,7-tetrakis (N, N -di-p-methoxyphenyl-amine) 9,9-spirobifluorene] (99.5%) was purchased from Feiming Science and Technology Co., Ltd Luminescence Technology Corp. All chemicals were used as received.

View Article Online
DOI: 10.1039/C8TA09026B

Devices fabrications

K chunks and rubrene powder were stored and handled in an argon-filled glove box (O_2 and H_2O <1 ppm), then transferred to a Pyrex ampoule at a molar ratio of 2:1. After sealed under vacuum (<10^{-4} mbar), the reactions were performed at 210 °C with a heating rate of 1 C/min and dwelling time of 3 days. Then the products were reground and re-pelletized for another 3-day reactions at the same temperatures to yield the final products K_2Rubrene.

The PSCs were prepared on FTO substrates with cleaned in detergent and then successively sonicated in deionized water, acetone, and isopropyl alcohol solution, then dried in an oven at 80°C. Prior to the deposition of electron transport layers (ETLs), FTO substrates was exposed to UV-ozone for 20 min. SnO_2 quantum dots (QDs) film was prepared according to the report of Fang et al.[45] Perovskite photoactive layers were deposited on ETLs by an anti-solvent method described in literatures.[20-22] The $(CsI)_{0.04}(FAI)_{0.82}(PbI_2)_{0.86}(MAPbBr_3)_{0.14}$ and $MAPbI_3$ precursor solutions were prepared in a glove-box from 1.35 M Pb^{2+} in a mixed solvent of DMF and DMSO (4:1 v/v). The dissolved solution was then spin-coated on FTO/SnO_2 QD ETLs substrate at 4500 rpm for 30 s in a glove box, note that 150 μL K_2Rubrene and rubrene chlorobenzene solution with 1mM concentrations was pipetted onto the spinning film at 15 s before the end of this program. Thereafter, the as-cast perovskite films were annealed at 150°C for 10 minutes. After cooling down to room temperature, spiro-OMeTAD solution (75 mg solved in 1 mL chlorobenzene) with 29 μL of TBP and 17.5 μL of Li-TFSI (520 mg mL^{-1} in acetonitrile) was spin-coated on the perovskite layer at

View Article Online
DOI: 10.1039/C8TA09026B

4000 rpm for 20 s in a glove box. Finally, gold was deposited by thermal evaporation on top of spiro-OMeTAD layer to complete the device, using a shadow mask to pattern the electrodes. The active area of the cells was 0.09 cm^2, which was defined by the area of the Au electrode.

Characterization

The J-V characteristics of the devices were measured using a B1500 A semiconductor parameter analyzer under the calibrated ABET Technologies SUN 2000 solar simulator equipped with an AM 1.5 filter at 100 mW/cm^2. The hole-only devices with the structure of FTO/PEDOT:PSS/K_2Rubrene(or rubrene)/Au is measured under dark ambient. Scanning was done at a scan rate of 0.1 Vs^{-1}. And the scans start and finish under forward bias and have 2 seconds stabilization time at forward bias under illumination prior to scanning. The corresponding incident photo-to-current efficiency (IPCE) spectrum was measured in air by a QE-R 3011 system from Enli Technology Co. Ltd. (Enli).

UV-visible spectroscopy was performed by using a UV–VIS–NIR spectrophotometer (UV-2550 Shimadzu) in the 200–800 nm wavelength range at room temperature. Fourier transform infra-red (FTIR) spectrum was recorded with a reflectance (ATR) instrument (PerkinElmer Spectrum 100, USA) from 4000 to 800 cm^{-1} with a resolution of 2 cm^{-1}.X-ray diffraction (XRD) patterns was determined by using a Rigaku SmartLab X-ray diffractometer with Cu Kα radiation. The morphologies of PSCs were investigated by a high-resolution field emission scanning electron

View Article Online
DOI: 10.1039/C8TA09026B

microscope (SEM, JSM7100F). Based on the tapping mode atomic force microscopy (AFM, Bruker NanoScope MultiMode 8.) system, the electrostatic force microscopy (EFM) measures simultaneously contact potential difference (CPD) between the probe (Nanosenser PPP-EFM) and surface of a perovskite sample by constantly probing. In our EFM measurement, a two-pass technique with phase mode was employed. The first pass was used to acquire the topographic height, and then the conductive probe was lifted with respect to the specimen surface with a constant separation, approximately 10 nm here, and scanned to acquire the potential offset between the tip and the sample. The first resonant oscillation of the cantilever (52.590 kHz) was used for the non-contact AFM topographic imaging. The second resonant frequency (60 kHz) was used for the potential imaging. We chose a scan rate of 0.977 Hz and a DC bias of 1 V applied to the conductive probe. The sample was fixed in a custom-made vertical sample holder with electrical connections to both electrodes. For Photothermal deflection absorption spectroscopy (PDS) measurement, the perovskite film was deposited on quartz substrate and then immersed into FC-72. A monochromatic light beam was modulated at 13 Hz by a mechanical chopper and shined onto the sample. A laser was at the perpendicular side so that it was deflected periodically. A position detector, connected with a lock-in amplifier, was placed on the other side so that the deflection signal was measured. Photoluminescence (PL) spectrum and Time-resolved photoluminescence (TRPL) signals of perovskite film were recorded by using Edinburgh FLSP920 spectrophotometer equipped with the excitation source of 485 nm picosecond pulsed diode laser.

View Article Online
DOI: 10.1039/C8TA09026B

Results and discussion

The synthesis of metal-organic complexing compound K_2Rubrene is under an inert ambient with potassium chunks and rubrene powder as raw materials. K_2Rubrene shows a monoclinic structure (Fig. 1a), and the detail crystal structure will be published elsewhere. K_2Rubrene crystal structure is different from that of rubrene with an orthorhombic symmetry (Space group: Cmca(65)) of a = 26.860 (10), b = 7.193 (3), and c = 14.433 (5) Å(Fig. S1).[46] The FTIR spectra are shown in lines in Fig. 1b. For rubrene, the peaks at 1622, 1596, 1574, 1494, 1464, 1439, 1411, and 1392 cm^{-1} can be assigned to the skeletal vibration of ring. In the low-frequency region, the peaks that are assigned to out-of-plane CH vibrations centered at 1309, 1270, 1214, 1171, 1152, 1128, 1107, 1067, 1026, 1001, 968, 910, and 848 cm^{-1} and that arise from the CH out-of-plane bending bands in the interval from 800 to 440 cm^{-1} (absorption bands centered at 789, 767,753, 733, 718, 694, 626, 614, 600, 583, 560, 545, 530, 509, 485, 464, and 444 cm^{-1}) are observed.[47] With the intercalation of potassium to form K_2Rubrene, the position of FTIR peaks changes much more. The ring skeletal vibration peaks arise at 1609, 1589, 1570, 1486, 1464, 1435, 1408, and 1373 cm^{-1}, which has shift towards low wave number, compared to that of rubrene. Most of the CH vibrations peaks at 1312, 1276, 1205, 1175, 1146, 1134, 1110, 1067, 1026, 997, 975, 907, 832 cm^{-1} shifts towards high wave number. However, most of the CH bending vibration peaks at 789, 767, 754, 738, 711, 692,626, 608, 600, 574, 560, 545, 530, 509, 480, 455, 444 cm^{-1} has no shift. These changes could be due to the twist of fusion rings induced by potassium intercalation. Specially, several new peaks (1544, 1522, 1355, 1089, 1039, 940, 892,

View Article Online
DOI: 10.1039/C8TA09026B

874, and 516 cm^{-1}) suggest the successful intercalation of potassium into rubrene. In K_2Rubrene, the reorientation of rubrene molecules to creates extra voids to accommodate potassium cations.[48]

At room temperature, rubrene has a high field-induced hole-mobility of up to 20 $cm^2V^{-1}s^{-1}$.[49, 50] Its highest occupied molecular orbital (HOMO) and lowest unoccupied molecular orbital (LUMO) are 5.4 and 3.0 eV, respectively.[51] Recently, it has been reported that some potassium-intercalated polyaromatic hydrocarbons show the metallic conductivity.[52, 53] Therefore, potassium intercalation can change the hole conductivity of rubrene, and thus benefit the hole-transport and -collection in PSCs.

The hole mobility values are measured using the space charge limited current (SCLC) method. We have fabricated hole-only devices (FTO/ PEDOT:PSS/K_2Rubrene(or rubrene)/Au) to measure the hole trap-state density in antisolvent dopants. Fig. 1c shows the double-logarithmic plot of dark J–V curves of the devices based on K_2Rubrene and rubrene. The linear J–V characteristics (blue) at low bias voltage indicates an ohmic response of the hole-only device. The super-linear J–V behavior at high bias voltage is the so-called SCLC where the electrode injects more carrier than what the material can transport, which can result in a net carrier distribution in the material.[54] The current-voltage curves of the hole-only devices are well fitted by the Mott-Gurney law (the blue and olive lines in Fig. 1c). Both the wider voltage range of ohmic response (at low bias voltage) and the smaller magnitude of the slope (at high bias voltage) from the fitted curve shows the material's superior carrier

View Article Online
DOI: 10.1039/C8TA09026B

transfer ability. Compared to the rubrene-based hole-only device, the K_2Rubrene based hole-only device has a bigger voltage range of ohmic response and the smaller slope (Fig. 1c), which infers potassium-intercalated rubrene has superior property of hole transferring than rubrene.

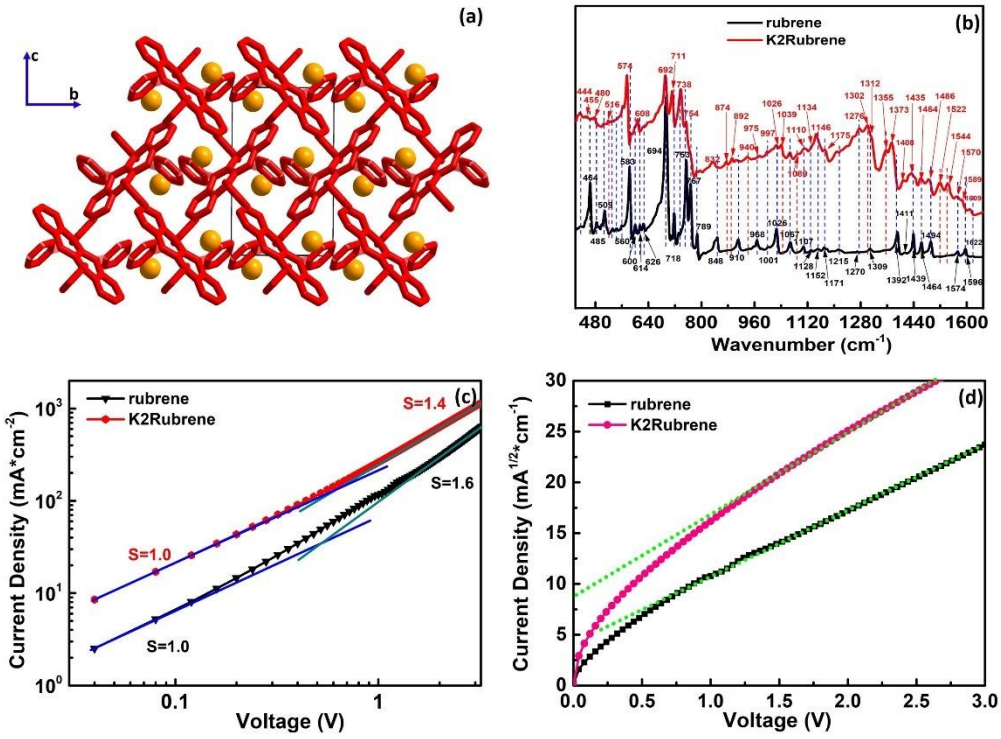

Fig. 1 (a) Crystal structure of K_2Rubrene, (b) FTIR absorption spectra of rubrene and K_2Rubrene, (c) Double-logarithmic plot of dark J–V characteristics from hole-only devices (FTO/PEDOT:PSS /K_2Rubrene(or rubrene)/Au), and the slopes of the blue and yellow lines marks at low and high bias voltage regime, respectively. And (d) $J^{1/2}$–V characteristics for SCLC hole-only mobility.

The hole mobility from the hole-only devices can be extracted from the dark current density–voltage curve (Fig. 1d), and is calculated by the trap free SCLC model ($J = \frac{9}{8}\varepsilon_0\varepsilon_r\mu\frac{V^2}{L^3}$, where ε_0 is the vacuum permittivity, ε_r is the dielectric constant, μ is the mobility of charge carrier, V is the effective applied voltage, and L is the thickness of the function layer.) at higher reverse applied voltage. K_2Rubrene shows a

View Article Online
DOI: 10.1039/C8TA09026B

hole mobility of 4.72×10^{-4} $cm^2V^{-1}s^{-1}$, larger than that of rubrene (1.40×10^{-4} $cm^2V^{-1}s^{-1}$). The higher mobility is likely caused by the K+-π interactions in the intercalated rubrene.

With K_2Rubrene and rubrene additives dissolved in CB antisolvent to for high quality perovskite films, PSCs with the structure of fluorine-doped tin oxide (FTO)/SnO_2 QD (30 nm)/perovskite (600 nm)/Spiro-OMeTAD (120 nm)/Au (130 nm) are fabricated, as shown in Fig. 2a. The corresponding cross-sectional SEM image is shown in shown in Fig. S2. By optimization, the concentration of 1.0 mM K_2Rubrene in the anti-solvent CB is the optimal performance result for the PSCs (Fig. S3). And the parameters of the corresponding devices derived from the current density (J) -voltage (V) characteristic curves (Fig. 2b) are summarized in Table 1.

TABLE 1. Summary of the J−V parameters the device with 1.0 mM rubrene and K_2Rubrene dissolved in the anti-solvent CB. The delay time was preset at 50ms with the voltage step of 0.02 V for J-V measurement. There are over 18 samples for every kind of device in this study.

Device Structure	Direction	*PCE* (%)	V_{oc} (V)	J_{sc} (mA/cm^2)	*FF* (%)	*HI(*)*
Control device	reverse-scan	17.82±0.56	1.10±0.01	21.59±0.34	75.0±0.5	0.237
	forward-scan	13.60±0.85	0.97±0.03	21.59±0.30	64.9±1.2	
CB with rubrene	reverse-scan	16.43±0.63	1.08±0.01	21.56±0.28	70.6±0.7	0.225
	forward-scan	12.73±0.91	0.93±0.02	21.54±0.33	63.4±1.8	
CB with K_2Rubrene	reverse-scan	18.14±0.67	1.10±0.01	21.85±0.31	75.4±1.0	0.023
	forward-scan	18.56±0.58	1.12±0.01	21.85±0.27	75.4±0.4	

(*) Hysteresis Index = $(PCE_{Rev}- PCE_{Fw})/PCE_{Rev}$

The control device has a reverse scan PCE of 17.82%, with open-circuit voltage (V_{OC}), short-circuit current density (J_{SC}), and fill factor (*FF*) of 1.10 V, 21.59 mA/cm^2, and 75.0% respectively, as showed in Table 1. With rubrene dissolved in anti-solvent CB, the PCE, J_{SC}, V_{OC}, and FF decrease to 16.43%, 21.56 mA/cm^2 1.08 V and 70.6%, respectively. For the K_2Rubrene-based device, the corresponding PCE, V_{OC}, J_{SC}, and

View Article Online
DOI: 10.1039/C8TA09026B

FF are improved to 18.56%, 1.12 V, 21.85 mA/cm^2, and 75.4%, respectively. The champion K_2Rubrene containing PSC has PCE up to 19.09% (Fig. S4). J_{SC} of the control device is bigger than that of the rubrene-based device, but smaller than that of the K_2Rubrene-based device, which is confirmed by the result of the corresponding incident photo-to-current efficiency (IPCE) (Fig. 2c). After illuminating under 1 sun for 200s, the control device shows a 17.52% stable PCE with a little fluctuation. The rubrene-based device presents the same steady state output beside a smaller stable PCE of 15.77%. For the K_2Rubrene-based device, its stable PCE is over 18%, and presents a firstly decreasing and then increasing trend (Fig. 2d). Obviously, measurements on a single J-V loop of the control and rubrene-treated device exhibit a commonly observed hysteresis behavior, with large hysteresis index (HI = (PCE_{Rev}- PCE_{Fw})/ PCE_{Rev}) of 0.237 and 0.225 respectively. For the K_2Rubrene-based device, however, the hysteresis behavior is much less, with a HI of only 0.023, i.e., over an order less that the other two cases. The tests are under the same testing requirements with the voltage step of 0.02 V and delay time of 50 ms at a pre-biased 1.2 V for 1s (Fig. 2b) and show good reproducibility (Fig. 2e).

To find out the performance difference of the PSCs, we first measured the absorption of the three-type perovskite films. With rubrene and K_2Rubrene treatment under the same preparation process, the perovskite films exhibit the decreased absorption compared with that of the pristine perovskite film in the wavelength range of 500-680 nm (Fig. S5. Therefore, the bigger J_{SC} of the K_2Rubrene- based device is not due to more photon absorption, but could be attributed to the intercalation of

View Article Online
DOI: 10.1039/C8TA09026B

potassium into rubrene, which can enhance K_2Rubrene' ability to improve the hole-transferring or -collecting.

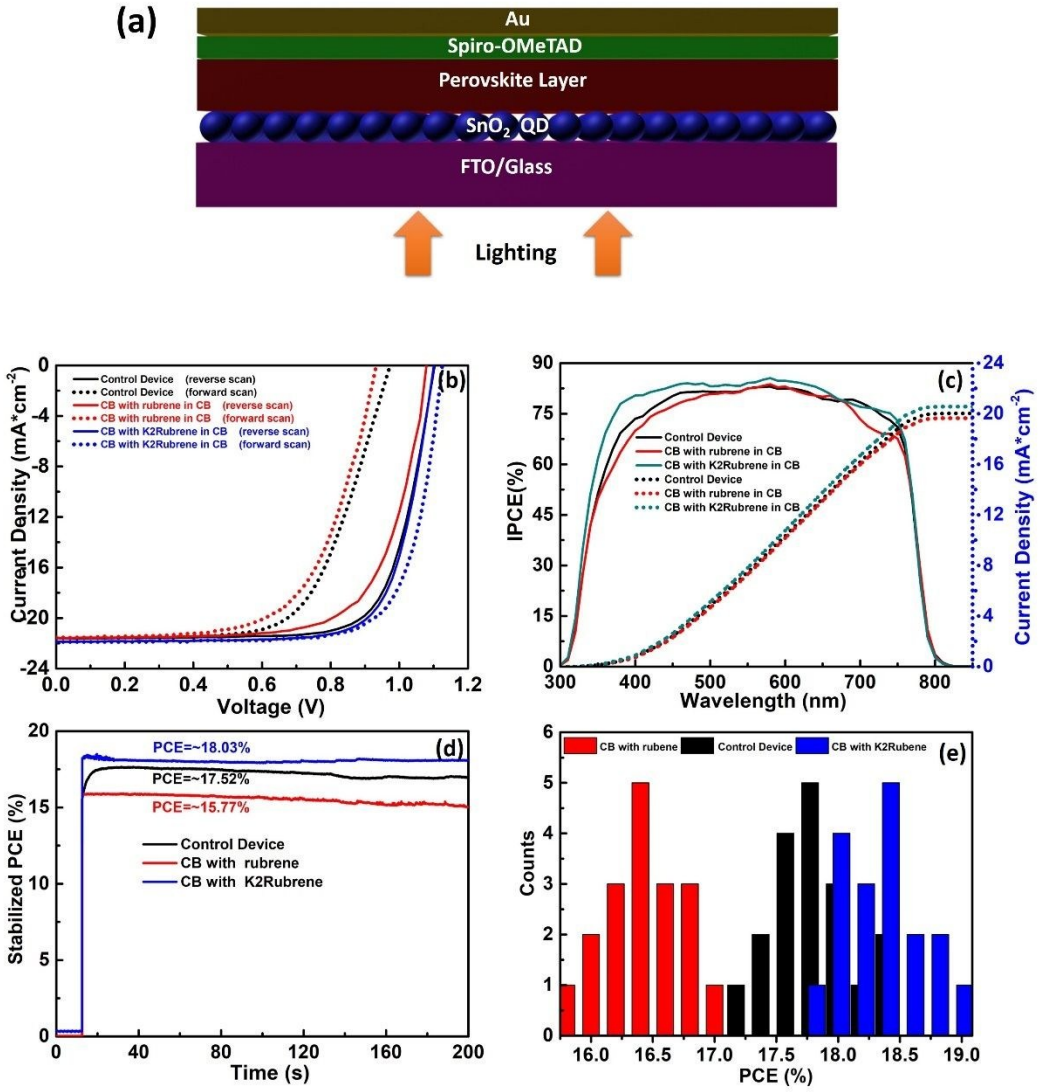

Fig. 2 (a) device structure, (b) the illuminated J–V characteristics, (c) IPCE, and (c) PCE as a function of time at a fixed voltage of the maximum power point (0.90 V) on the J-V curve (reverse scan, from open circuit to short circuit) for the device with rubrene and K_2Rubrene dissolved in anti-solvent CB. (d) Histogram of efficiencies based on 18 devices for each type PSC. The device without encapsulation is pre-biased at 1.2 V for 1 s with the voltage step and delay time of 0.02 V and 50ms respectively.

FTIR spectrum are employed to measure the change of various organic group with rubrene and K_2Rubrene treatment, as shown in Fig. S6. A strong stretching vibration of C=N appears at 1711 cm^{-1}, corresponding to the intrinsic characteristic peaks of organic

View Article Online
DOI: 10.1039/C8TA09026B

cation FA^+ groups of perovskites. The peaks at 1048 cm^{-1} and at 1616, 3160, 3272, 3332, 3358 & 3407 cm^{-1} are assigned to the C-N and N-H stretching vibration from FA^+/MA^+ groups, respectively. The absorption peaks at 1352 and 1472 cm^{-1} belong to the bending vibration of methyl (CH_3) from the MA^+ group. In two treated perovskite films, no peaks from rubrene or K_2Rubrene can be detected and there is no evident peak shift from organic groups, suggestive of very few additive materials to decorate the perovskite photoactive layer.

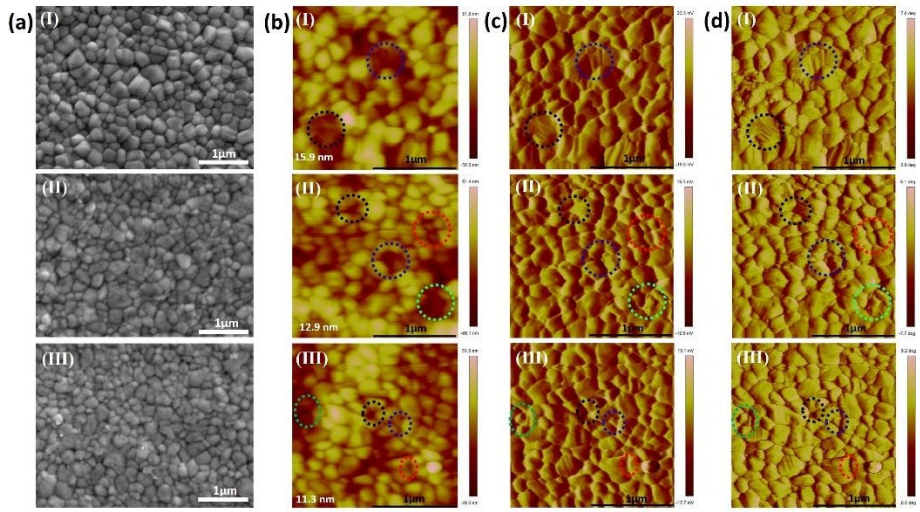

Fig. 3 (a) SEM images, and (b) Topography, (c) Amplitude, & (d) Phase in the EFM images of the mixed ternary cation perovskite films: (Ⅰ) the pristine perovskite film and the perovskite films with (Ⅱ) rubrene and (Ⅲ) K2Rubrene treatment.

Top-view SEM images reveal stark differences of perovskite films with rubrene and K_2Rubrene additives (Fig. 3a). The pristine film is well crystallized and composed of many relatively large (ca. 500 nm) crystals filled with ca.150 nm small crystals (Fig. 3a(Ⅰ)). With rubrene and K_2Rubrene additives, the crystal grain size decreases substantially and subtly without pinholes, and their surfaces seem not so glossy as the pristine film (Fig. 3a (Ⅱ, Ⅲ)). It implies that rubrene and K_2Rubrene could hinder the

View Article Online
DOI: 10.1039/C8TA09026B

diffusivity of the perovskite precursor and trigger a crucial impact on the nucleation over the perovskite precursor film during the process of solvent drying stage. Interestingly, the distribution of grain size triggered by K_2Rubrene is more homogeneous and uniform than that triggered by rubrene. Thus, potassium ion should take part in the formation of perovskite film.

To further scrutinize the uniformity of treated perovskite film, we performed phase mode EFM measurement to assess simultaneously the surface topography and the amplitude of perovskite film between the tip and the sample (Fig. 3b-d). The amplitude corresponds to the electrostatic force field, which is proportional to the surface CPD between GBs and inner grains in a perovskite films.[55] This measurement can help to reveal the relationship between traps and carrier transfer around the GBs with foreign bodies doping.[28] The EFM topographies show that the apparent grain size is consistent with that shown in the SEM images (Fig. 3a), and the roughness is reduced from 15.9 to 12.9 nm and 11.3 nm in rubrene- and K_2Rubrene- treated perovskite films, respectively (Fig. 3b). Obviously rubrene and K_2Rubrene can control nucleation and slow down the crystal growth to obtain the uniform perovskite films, and they mainly accumulate at GBs. EFM measurement is conducted under dark ambient conditions to avoid the excess charges. The CPD should be constant across the film surface and correspond to the work function difference between the tip and FTO substrates.[56] Thus, any change in amplitude indicate the presence of an internal field inside the device. In Fig. 3b, some dark areas present in topography images at GBs, but the corresponding area shows bright in amplitude images (Fig. 3c). Especially, there are obviously

View Article Online
DOI: 10.1039/C8TA09026B

difference in the area with dash circle marked. This could be due to the built-in potential resulted from the interstitials and vacancies at the GBs.[56-59] Moreover, the polarity at GBs can be different from that inside grains, leading to different CPD values.[28] Although the individual grains are clearly distinguishable in morphology and amplitude images, the shape is not identical. In rubrene and K_2Rubrene treated perovskite film, the difference becomes more evident, likely due to the lower built-in potential around charged GBs induced by changed carrier distribution resulted from the cation–π interaction between aromatic additive and the organic cations. Under a bias voltage, these organic additives of high carrier-mobility/conductivity change the electrostatic force field distribution of the surface of perovskite. Stranks and coworkers have reported that potassium selectively depletes bromide from the perovskite crystal structure at the GBs and surfaces.[35] Some interface traps, such as the dangling bonds and vacancies, could be "digested" by potassium cations, and smooth the surface of perovskite film further and redistribute the electrostatic force field. These could result in a minimized recombination for the better carrier transfer at GBs.

Table 2 Fitting Decay Times of the mixed ternary cation perovskite films prepared by anti-solvent method with rubrene and K_2Rubrene in CB.

Samples	τ_1(ns)	Fraction1	τ_2(ns)	Fraction2
Quartz\Perovskite (CB without additive)	3.0±0.1	76.7%	94±1	23.3%
Quartz\Perovskite (CB with rubrene)	1.6±0.2	89.4%	70±4	10.6%
Quartz\Perovskite (CB with K_2Rubrene)	1.2±0.1	99.9%	28±2	0.1%

To estimate charge collection efficiency, the corresponding PL spectra are measured, as shown in Fig. 4a. All perovskite films display an emission peak at 778 nm. The quenched PL spectra in treated films indicate the existence of a "bulk organic

View Article Online
DOI: 10.1039/C8TA09026B

molecular layer". As we know, the PL intensity and carrier's life time will be increased with the light scattering effect of better-quality perovskite- pinhole free and dense film. Moreover, the "bulk organic molecular layer" could form the cation–π interaction with the adjacent organic cations of perovskites at the rubrene(or K_2Rubrene)/perovskite-photoactive-layer interface or GBs, which can immobilize the organic cations of perovskite and thus passivate the defects on the surface (or GBs) of perovskite layer, leading to the better carrier transfer in the perovskite layer.[44] The K_2Rubrene-treated film exhibits a smaller PL spectra intensity than that of the rubrene treated film, suggestive of the superior passivation function of K intercalation to improve effectively the hole transfer. To better understand the enhanced performance by rubrene and K_2Rubrene treatment, we further employed the time-resolved photo-luminescence decay (TRPL) to measure the carrier lifetime (shown in Fig. 4b). All curves are fitted with two-component exponential decay according to previous report.[60, 61] The fast decay PL species (τ_1) can be attributed to quenching via trap states or interfacial charge transfer, and the longer PL species (τ_2) is attributed to the free carrier recombination via the light emission.[61] In the pristine film, the fast decay PL species (τ_1) and the longer PL species (τ_2) are 3.0 (76.7%) and 94 (23.3%) ns, respectively (**Table 2**). In rubrene-treated film, the fast decay PL species τ_1 is the dominated characteristic and its fraction (τ_1) increases immediately from 76.7 to 99.9%, which is attributed to the construction of more cation–π interaction through the perovskite and rubrene interfaces. The decreased τ_1 indicates that the rubrene treatment could passivate the surface defects of perovskite, which suggests rapid hole-transferring from perovskite to rubrene. In pure

View Article Online
DOI: 10.1039/C8TA09026B

perovskite film, the slower τ_2 is related with a better carrier lifetime in the perovskite film. In the rubrene treated perovskite film, although the τ_2 component decreases with rubrene, the decreases of τ_2 from 94 ns in neat perovskite film to 70 ns may indicate that rubrene gives full play to the role of hole-collecting and provides more pathways for hole to transfer from perovskite to rubrene due to the formation of cation–π interaction at the larger interfaces. [62, 63] In the K_2Rubrene-treated film, the lifetimes of fast and slower decay PL species decrease further. The fraction of fast specie (τ_1) increases further to 99.9%, which could be attributed to the synergy of the cation–π interaction between perovskite and rubrene and the complex interaction between potassium cation and perovskite (Fig. 4c).

Thus, K_2Rubrene can passivate the defects in perovskite layer more effectively, enable fast hole transfer from the perovskite layer to anode, and suppress effectively the recombination at the Spiro-OMeTAD/perovskite interface, accounting for the increase in the V_{oc}, J_{sc}, and the decrease of hysteresis.

The star-marked XRD peaks are the characteristic of a trigonal (Space group: P3m1 (156)) perovskite phase (Fig. S7) [64, 65]. The peak at 12.5° is from PbI_2 in the perovskite film. With rubrene and K_2Rubrene additives, the PbI_2 peak intensity decreases, indicating smaller density of defects and more stable crystal frameworks of perovskites. The K_2Rubrene-treated film shows the smallest PbI_2 peak intensity among the three type samples, demonstrating that K^+ could prevent the degeneration of perovskite film by passivating the dangling bonds at the surface/interface or GBs within

View Article Online
DOI: 10.1039/C8TA09026B

perovskite film, because K^+ energetically prefers the interstitial site.[66]

PDS measurements are performed to probe the effect of potassium cation incorporation and interaction with rubrene on the perovskite films, as presented in Fig. 4d. According to the direct transition type Tauc-plot,[67] three perovskite film samples have the same band gap of ca.1.58 eV, which is in excellent agreement with previous reports.[28] The Urbach energy can be used to identify the shallow traps, and its magnitude reflects the figure-of-merit for the film. A small Urbach energy stipulates a lower density of shallow traps,[68, 69] and results in the little non-radiative recombination at the interface contacts or GBs of the bulk perovskite semiconductor. The Urbach energy increases from 23.4 meV of the pristine perovskite sample to 24.1 meV in rubrene-treated films, decreases to 23.3 meV K_2Rubrene-treated films, suggesting that K_2Rubrene treatment can lead to the substantial passivation of sub-bandgap states compared to rubrene treatment.

View Article Online
DOI: 10.1039/C8TA09026B

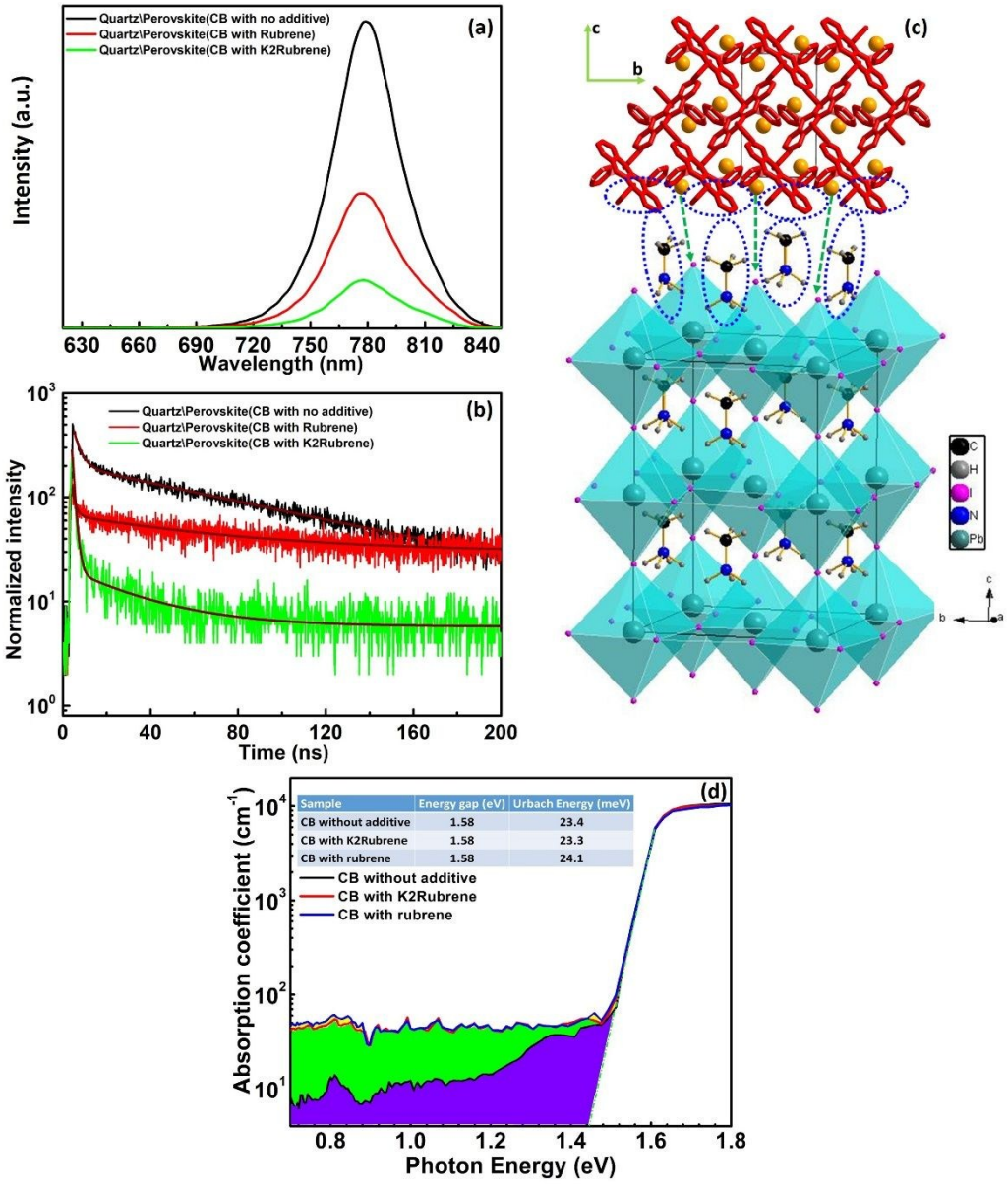

Sample	Energy gap (eV)	Urbach Energy (meV)
CB without additive	1.58	23.4
CB with K2Rubrene	1.58	23.3
CB with rubrene	1.58	24.1

Fig. 4. (a) Steady state PL, (b) TRPL, (c) Schematic illustration of the potential surface defect sites, and (d) PDS spectra of the mixed ternary cation perovskite films prepared by anti-solvent method with rubrene and K_2Rubrene dissolved in antisolvent CB. The violet region indicates the deep trap states of the pristine sample, the sum of green and violet region indicates the deep trap states of the sample with K_2Rubrene treated, and the sum of yellow, green and violet region indicates the deep trap states of the sample with rubrene treated. The 485 nm laser is directly on the sample for PL and TRPL test.

It has been reported that the migration & autorotation of the large organic cations in the vicinity of the lattice grid can be inclined to generate the A-site defects, which play very vital functions on the hybrid perovskite's electric structures as well as the

View Article Online
DOI: 10.1039/C8TA09026B

device performance.[70] Any halide vacancies at GBs could result in the halide migration and the additional non-radiative decay.[35] Park et al. have declared that K^+ is able to prevent the formation of Frenkel defect because K^+ energetically prefers the interstitial site.[66] Such a low level of energetic disorder indicates that the potassium insertion to afford K_2Rubrene could "digest" the shallow traps to prevent the migration & autorotation of the large organic cations (or the migration of halide) at interface between the HTL and the perovskite absorber, or perovskite/perovskite GBs (Fig. 4c), thereby suppressing any additional non-radiative decay and enhancing the carriers lifetime.[35, 71]

Unfortunately, the treatment of K_2Rubrene and rubrene increases the deep trap density between 0.7 and 1.5 eV on the surface of the perovskite film. Theoretical calculation shows a chelation-like interaction between MA^+ cations and rubrene: two N-H bonds in MA^+ toward rubrene hook the central tetracene and the pending phenyl group through $\sigma_{N\text{-}H}$*–π rubrene interactions, respectively.[44] And these different interaction energies demonstrates that the different interaction strength could lead to the disorder on the surface of perovskite film. Moreover, rubrene couldn't be compatible perfectly with perovskite structure due to its supramolecular structure, although these aromatic organics can immobilize the organic cations on the surface of perovskite. Thus, the K_2Rubrene-treated perovskite sample shows much higher density of deep-traps than the pristine perovskite sample. K^+ could enter freely the A-site defects at surface of the perovskite absorber to prevent the migration & autorotation of the large organic cations or the migration of halide. More importantly, K^+ insertion could balance the cation–π interaction between the aromatic additive and the organic

View Article Online
DOI: 10.1039/C8TA09026B

cations in perovskite films to reduce the barrier for the better carrier transfer at GBs. Consequently, a significant rise of valence band maximum (VBM) and conduction band minimum (CBM) of the perovskite material will lead to a more favorable energy alignment with hole transporting material at the interface between HTL and perovskite photoactive lay[72] (Fig. 5a&b), which can suppress the hysteresis for the better properties of PSC.

Tress et al. believe that the slow process, including ion migration and changing dipole charge at interfaces, is the origin of the hysteresis.[73] The lower charge carrier mobility and extraction rates are, the more prone is the device to exhibiting hysteresis. Although rubrene has a high field-induced hole-mobility,[49, 50] a notorious normal hysteresis index indicates that the rubrene's worse passivation compatibility at the interface between the spiro-OMeTAD and the perovskite absorber (or at perovskite/perovskite GBs[74, 75]) could result in the disequilibrium for the mobility of electron and hole during the work/test of device with rubrene-treated perovskite. Thus, the ionic charges could accumulate at cathode interface to present a bigger normal hysteresis behavior for PSC devices. With K_2Rubrene treatment, the upward valence band maximum could level up the barriers at the interface between perovskite and spiro-OMeTAD (Fig. 5b), which could increase the hole-mobility to reduce the charge accumulation at the perovskite/spiro-OMeTAD interface (Fig. 5c). Moreover, the defects, such as dangling bonds and vacancies, are passivated to improve the crystal quality of the perovskite film.

View Article Online
DOI: 10.1039/C8TA09026B

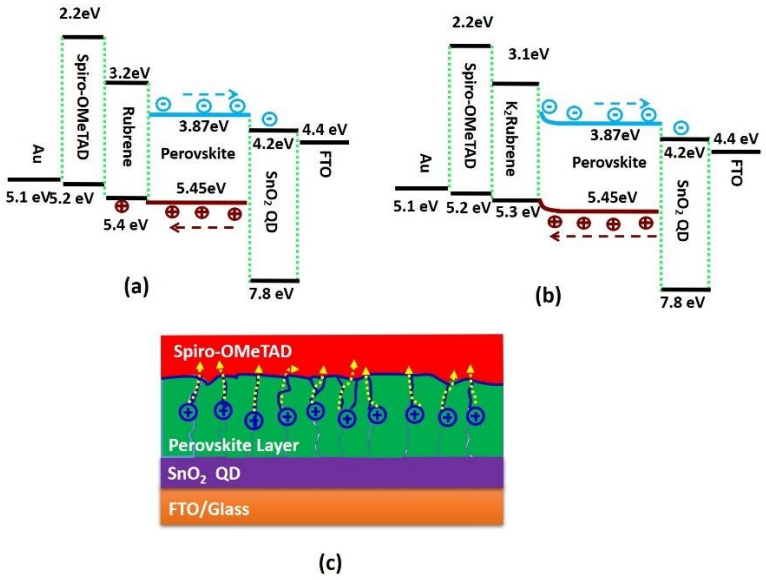

Fig. 5. Energy level diagram of PSC with (a) rubrene and (b) K_2Rubrene treatment, (c) The proposed hole-transport process of perovskite with rubrene and K_2Rubrene treatment passivation.

Conclusions

In summary, we introduce a facile anti-solvent engineering to obtain high quality perovskite film for high efficiency device with rubrene and K_2Rubrene passivation. It is found that the rubrene-based organics can immobilize the organic cations in perovskite by the cation–π interaction between aromatic rubrene and organic cations. This interaction can trigger heterogeneous nucleation over the perovskite precursor film and lead to smaller grain size and more homogeneous and uniform perovskite film. The potassium insertion in K_2Rubrene could balance the cation–π interaction between aromatic additive and the organic cations in perovskite films to reduce the barrier for the better carrier transfer at GBs. K^+ could also enter freely the A-site defects at surface of the perovskite absorber and then digest the A-site shallow defects to prevent the migration & autorotation of the large organic cations (or the migration of halide) at interface between the HTL and the perovskite absorber, or perovskite/perovskite GBs.

View Article Online
DOI: 10.1039/C8TA09026B

Consequently, a significant upshift of valence band maximum and conduction band minimum of the perovskite material lead to a more favorable energy alignment with hole transporting material, enhance the hole-transfer and suppress the hysteresis. The PSCs with the K_2Rubrene treatment yield a high efficiency over 19%, significantly larger than those of the pristine and rubrene based devices. This work demonstrates a promising passivation material concept for perovskite solar cells.

Conflict of interest

The authors declare no competing financial interest.

Acknowledgments

This work was supported by the funding from Research Grants Council of Hong Kong (Grant No. 15246816, and 15218517), the Project of Strategic Importance provided by the Hong Kong Polytechnic University (Project Code: 1-ZE29). This work is also supported by the Natural Science Foundation of Hubei Province (2014CFB275), the Science Foundation (K201827, K201504) of Wuhan Institute of Technology. The authors would like to thank professor Shu Kong So of Hongkong Baptist University for help with PDS measurement.

View Article Online
DOI: 10.1039/C8TA09026B

References

1. J. H. Im, C. R. Lee, J. W. Lee, S. W. Park and N. G. Park, *Nanoscale*, 2011, **3**, 4088-4093.
2. H.-S. Kim, C.-R. Lee, J.-H. Im, K.-B. Lee, T. Moehl, A. Marchioro, S.-J. Moon, R. Humphry-Baker, J.-H. Yum, J. E. Moser, M. Grätzel and N.-G. Park, *Sci. Rep.*, 2012, **2**, 591-598.
3. M. M. Lee, J. Teuscher, T. Miyasaka, T. N. Murakami and H. J. Snaith, *Science*, 2012, **338**, 643-647.
4. M. Liu, M. B. Johnston and H. J. Snaith, *Nature*, 2013, **501**, 395-398.
5. A. Kojima, K. Teshima, Y. Shirai and T. Miyasaka, *J. Am. Chem. Soc.*, 2009, **131**, 6050–6051.
6. W. S. Yang, B.-W. Park, E. H. Jung, N. J. Jeon, Y. C. Kim, D. U. Lee, S. S. Shin, J. Seo, E. K. Kim, J. H. Noh and S. I. Seok, *Science*, 2017, **356**, 1376–1379.
7. C. Zuo, H. J. Bolink, H. Han, J. Huang, D. Cahen and L. Ding, *Adv. Sci.*, 2016, **3**, 1500324.
8. S. Sun, T. Salim, N. Mathews, M. Duchamp, C. Boothroyd, G. Xing, T. C. Sum and Y. M. Lam, *Energy Environ. Sci.*, 2014, **7**, 399-407.
9. J.-Y. Jeng, Y.-F. Chiang, M.-H. Lee, S.-R. Peng, T.-F. Guo, P. Chen and T.-C. Wen, *Adv. Mater.*, 2013, **25**, 3727-3732.
10. J. Burschka, N. Pellet, S.-J. Moon, R. Humphry-Baker, P. Gao, M. K. Nazeeruddin and M. Gratzel, *Nature*, 2013, **499**, 316-319.
11. J.-H. Im, I.-H. Jang, N. Pellet, M. Grätzel and N.-G. Park, *Nat. Nano.*, 2014, **9**, 927-932.
12. S. Ito, S. Tanaka and H. Nishino, *J. Phys. Chem. Lett.*, 2015, **6**, 881-886.
13. O. Malinkiewicz, A. Yella, Y. H. Lee, G. M. Espallargas, M. Grätzel, K. Mohammad, Nazeeruddin and H. J. Bolink, *Nat. Photon.*, 2014, **8**, 128-132.
14. Q. Lin, A. Armin, R. C. R. Nagiri, P. L. Burn and P. Meredith, *Nat. photon.*, 2015, **9**, 106-112.
15. J. Borchert, H. Boht, W. Fränzel, R. Csuk, R. Scheer and P. Pistor, *J. Mater. Chem. A*, 2015, **3**, 19842-19849.
16. Q. Chen, H. Zhou, Z. Hong, S. Luo, H.-S. Duan, H.-H. Wang, Y. Liu, G. Li and Y. Yang, *J. Am. Chem. Soc.*, 2014, **136**, 622-625.
17. C.-W. Chen, H.-W. Kang, S.-Y. Hsiao, P.-F. Yang, K.-M. Chiang and H.-W. Lin, *Adv. Mater.*, 2014, **26**, 6647-6652.
18. C. Li, F. Wang, J. Xu, J. Yao, B. Zhang, C. Zhang, M. Xiao, S. Dai, Y. Li and Z. a. Tan, *Nanoscale*, 2015, **7**, 9771-9778.
19. H. Zhang, J. Cheng, D. Li, F. Lin, J. Mao, C. Liang, A. K.-Y. Jen, M. Grätzel and W. C. H. Choy, *Adv. Mater.*, 2017, **29**, 1604695.
20. D. Bi, C. Yi, J. Luo, J.-D. Décoppet, F. Zhang, Shaik M. Zakeeruddin, X. Li, A. Hagfeldt and M. Grätzel, *Nat. Energy*, 2016, **1**, 16142.
21. F. Zhang, W. Shi, J. Luo, N. Pellet, C. Yi, X. Li, X. Zhao, T. J. S. Dennis, X. Li, S. Wang, Y. Xiao, S. M. Zakeeruddin, D. Bi and M. Gratzel, *Adv. Mater.*, 2017, **29**, 1606806.
22. N. J. Jeon, J. H. Noh, Y. C. Kim, W. S. Yang, S. Ryu and S. I. Seok, *Nat. Mater.*, 2014, **13**, 897-903.
23. N. Ahn, D.-Y. Son, I.-H. Jang, S. M. Kang, M. Choi and N.-G. Park, *J. Am. Chem. Soc.*, 2015, **137**, 8696-8699.
24. Y. Wu, A. Islam, X. Yang, C. Qin, J. Liu, K. Zhang, W. Peng and L. Han, *Energy Environ. Sci.*, 2014, **7**, 2934-2938.
25. P.-W. Liang, C.-Y. Liao, C.-C. Chueh, F. Zuo, S. T. Williams, X.-K. Xin, J. Lin and A. K. Y. Jen, *Adv. Mater.*, 2014, **26**, 3748-3754.

26. Y. Wu, F. Xie, H. Chen, X. Yang, H. Su, M. Cai, Z. Zhou, T. Noda and L. Han, *Adv. Mater.*, 2017, **29**, 1701073.
27. W. Ke, C. Xiao, C. Wang, B. Saparov, H.-S. Duan, D. Zhao, Z. Xiao, P. Schulz, S. P. Harvey, W. Liao, W. Meng, Y. Yu, A. J. Cimaroli, C.-S. Jiang, K. Zhu, M. Al-Jassim, G. Fang, D. B. Mitzi and Y. Yan, *Adv. Mater.*, 2016, **28**, 5214-5221.
28. P. L. Qin, G. Yang, Z. w. Ren, S. H. Cheung, S. K. So, L. Chen, J. Hao, J. Hou and G. Li, *Adv. Mater.*, 2018, **30**, 1706126.
29. Z. Liu, L. Zhang, M. Shao, Y. Wu, D. Zeng, X. Cai, J. Duan, X. Zhang and X. Gao, *ACS Appl. Mater. Inter.*, 2018, **10**, 762-768.
30. M. Saliba, T. Matsui, K. Domanski, J.-Y. Seo, A. Ummadisingu, S. M. Zakeeruddin, J.-P. Correa-Baena, W. R. Tress, A. Abate, A. Hagfeldt and M. Grätzel, *Science*, 2016, **354**, 206-209.
31. S. Bag and M. F. Durstock, *ACS Appl. Mater. Inter.*, 2016, **8**, 5053-5057.
32. W. Zhao, D. Yang and S. F. Liu, *Small*, 2017, **13**, 1604153.
33. C. Zuo and L. Ding, *Nanoscale*, 2014, **6**, 9935-9938.
34. J. T.-W. Wang, Z. Wang, S. Pathak, W. Zhang, D. W. deQuilettes, F. Wisnivesky-Rocca-Rivarola, J. Huang, P. K. Nayak, J. B. Patel, H. A. Mohd Yusof, Y. Vaynzof, R. Zhu, I. Ramirez, J. Zhang, C. Ducati, C. Grovenor, M. B. Johnston, D. S. Ginger, R. J. Nicholas and H. J. Snaith, *Energ. Environ. Sci.*, 2016, **9**, 2892-2901.
35. M. Abdi-Jalebi, Z. Andaji-Garmaroudi, S. Cacovich, C. Stavrakas, B. Philippe, J. M. Richter, M. Alsari, E. P. Booker, E. M. Hutter, A. J. Pearson, S. Lilliu, T. J. Savenije, H. Rensmo, G. Divitini, C. Ducati, R. H. Friend and S. D. Stranks, *Nature*, 2018, **555**, 497.
36. H.-L. Hsu, H.-T. Hsiao, T.-Y. Juang, B.-H. Jiang, S.-C. Chen, R.-J. Jeng and C.-P. Chen, *Adv. Energy Mater.*, **0**, 1802323.
37. Z. Liu, Y. Wu, Q. Zhang and X. Gao, *J. Mater. Chem. A*, 2016, **4**, 17604-17622.
38. B. Xu, Z. Zhu, J. Zhang, H. Liu, C.-C. Chueh, X. Li and A. K. Y. Jen, *Adv. Energy Mater.*, 2017, **7**, 1700683.
39. D. Liu, J. Yang and T. L. Kelly, *J. Am. Chem. Soc.*, 2014, **136**, 17116-17122.
40. M. Li, Z.-K. Wang, Y.-G. Yang, Y. Hu, S.-L. Feng, J.-M. Wang, X.-Y. Gao and L.-S. Liao, *Adv. Energy Mater.*, 2016, **6**, 1601156.
41. T. Miletic, E. Pavoni, V. Trifiletti, A. Rizzo, A. Listorti, S. Colella, N. Armaroli and D. Bonifazi, *ACS Appl. Mater. Inter.*, 2016, **8**, 27966-27973.
42. G. Dong, D. Xia, Y. Yang, L. Shenga, T. Ye and R. Fan, *ACS Appl. Mater. Inter.*, 2017, **9**, 2378-2386.
43. E. J. Juarez-Perez, M. R. Leyden, S. Wang, L. K. Ono, Z. Hawash and Y. Qi, *Chem. Mater.*, 2016, **28**, 5702-5709.
44. D. Wei, F. Ma, R. Wang, S. Dou, P. Cui, H. Huang, J. Ji, E. Jia, X. Jia, S. Sajid, A. M. Elseman, L. Chu, Y. Li, B. Jiang, J. Qiao, Y. Yuan and M. Li, *Adv. Mater.*, 2018, **30**, 1707583.
45. G. Yang, C. Chen, F. Yao, Z. Chen, Q. Zhang, X. Zheng, J. Ma, H. Lei, P. Qin, L. Xiong, W. Ke, G. Li, Y. Yan and G. Fang, *Adv. Mater.*, 2018, **30**, 1706023.
46. O. D. Jurchescu, A. Meetsma and T. T. M. Palstra, *Acta Crystallogr. Sect. B*, 2006, **62**, 330-334.
47. R. Fedorovych, T. Gavrilko, YA. Lopatina, A. Marchenko, V. Nechytaylo, A. Senenko, L. Viduta and J. Baran, *Ukr. J. Phys.*, 2016, **61**, 547-555.
48. F. D. Romero, M. J. Pitcher, C. I. Hiley, G. F. S. Whitehead, S. Kar, A. Y. Ganin, D. Antypov, C. Collins, M. S. Dyer, G. Klupp, R. H. Colman, K. Prassides and M. J. Rosseinsky, *Nat. Chem.*, 2017,

View Article Online
DOI: 10.1039/C8TA09026B

9, 644-652.

49. D. A. da Silva Filho, E. G. Kim and J. L. Brédas, *Adv. Mater.*, 2005, **17**, 1072-1076.
50. V. Podzorov, E. Menard, A. Borissov, V. Kiryukhin, J. A. Rogers and M. E. Gershenson, *Phys. Rev. Lett.*, 2004, **93**, 086602.
51. J. Huang, Y. Qi, H. Wang and J. Yu, *Appl. Phys. Lett.*, 2013, **102**, 183302.
52. M. F. Craciun, G. Giovannetti, S. Rogge, G. Brocks, A. F. Morpurgo and J. van den Brink, *Phys. Rev. B*, 2009, **79**, 125116.
53. T. Minakata, M. Ozaki and H. Imai, *J. Appl. Phys.*, 1993, **74**, 1079-1082.
54. P. Qin, G. Fang, W. Zeng, X. Fan, Q. Zheng, F. Cheng, J. Wan and X. Zhao, *Sol. Energy Mater. Sol. Cells*, 2011, **95**, 3311-3317.
55. S. Lilliu, C. Maragliano, M. Hampton, M. Elliott, M. Stefancich, M. Chiesa, M. S. Dahlem and J. E. Macdonald, *Sci Rep*, 2013, **3**, 3352.
56. J. S. Yun, A. Ho-Baillie, S. Huang, S. H. Woo, Y. Heo, J. Seidel, F. Huang, Y. B. Cheng and M. A. Green, *J. Phys. Chem. Lett.*, 2015, **6**, 875-880.
57. R. A. De Souza, *Phys. Chem. Chem. Phys.*, 2009, **11**, 9939-9969.
58. H. Hilgenkamp, J. Mannhart and B. Mayer, *Physical Review B*, 1996, **53**, 14586-14593.
59. R. F. Klie, M. Beleggia, Y. Zhu, J. P. Buban and N. D. Browning, *Phys. Rev. B*, 2003, **68**, 214101.
60. Q. Chen, H. Zhou, T. B. Song, S. Luo, Z. Hong, H. S. Duan, L. Dou, Y. Liu and Y. Yang, *Nano Lett.*, 2014, **14**, 4158-4163.
61. L. Zuo, Q. Chen, N. De Marco, Y. T. Hsieh, H. Chen, P. Sun, S. Y. Chang, H. Zhao, S. Dong and Y. Yang, *Nano Lett.*, 2017, **17**, 269-275.
62. M. Zhang, J. Wang, L. Li, G. Zheng, K. Liu, M. Qin, H. Zhou and X. Zhan, *Adv. Sci.*, 2017, **4**, 1700025.
63. Y. Liu, Q. Chen, H.-S. Duan, H. Zhou, Y. Yang, H. Chen, S. Luo, T.-B. Song, L. Dou, Z. Hong and Y. Yang, *J. Mater. Chem. A*, 2015, **3**, 11940-11947.
64. N. J. Jeon, J. H. Noh, W. S. Yang, Y. C. Kim, S. Ryu, J. Seo and S. I. Seok, *Nature*, 2015, **517**, 476-480.
65. C. C. Stoumpos, C. D. Malliakas and M. G. Kanatzidis, *Inorg. Chem.*, 2013, **52**, 9019-9038.
66. D.-Y. Son, S.-G. Kim, J.-Y. Seo, S.-H. Lee, H. Shin, D. Lee and N.-G. Park, *J. Am. Chem. Soc.*, 2018, **140**, 1358-1364.
67. J. Tauc, *Mater. Res. Bull.*, 1968, **3**, 37-46.
68. A. Ng, Z. Ren, Q. Shen, S. H. Cheung, H. C. Gokkaya, S. K. So, A. B. Djurisic, Y. Wan, X. Wu and C. Surya, *ACS Appl. Mater. Inter.*, 2016, **8**, 32805-32814.
69. J. A. Carr and S. Chaudhary, *Energ. Environ. Sci.*, 2013, **6**, 3414-3438.
70. P. Zhao, W. Yin, M. Kim, M. Han, Y. J. Song, T. K. Ahn and H. S. Jung, *J. Mater. Chem. A*, 2017, **5**, 7905-7911.
71. T. Bu, X. Liu, Y. Zhou, J. Yi, X. Huang, L. Luo, J. Xiao, Z. Ku, Y. Peng, F. Huang, Y.-B. Cheng and J. Zhong, *Energ. Environ. Sci.*, 2017, **10**, 2509-2515.
72. D. Yao, C. Zhang, N. D. Pham, Y. Zhang, V. T. Tiong, A. Du, Q. Shen, G. J. Wilson and H. Wang, *J. Phys. Chem. Lett.*, 2018, **9**, 2113-2120.
73. W. Tress, J. P. Correa Baena, M. Saliba, A. Abate and M. Graetzel, *Adv. Energy Mater.*, 2016, **6**, 1600396.
74. J. Peng, Y. Wu, W. Ye, D. A. Jacobs, H. Shen, X. Fu, Y. Wan, T. Duong, N. Wu, C. Barugkin, H. T. Nguyen, D. Zhong, J. Li, T. Lu, Y. Liu, M. N. Lockrey, K. J. Weber, K. R. Catchpole and T. P. White,

Energy. Environ. Sci., 2017, **10**, 1792-1800.

View Article Online
DOI: 10.1039/C8TA09026B

75. X. Zheng, B. Chen, J. Dai, Y. Fang, Y. Bai, Y. Lin, H. Wei, Xiao C. Zeng and J. Huang, *Nat. Energy*, 2017, **2**, 17102.